Application of Hybrid Laser Powder Bed Fusion Additive Manufacturing to Microwave Radio Frequency Quarter Wave Cavity Resonators

Alex Riensche^{1,2}, Paul Carriere³, Ziyad Smoqi¹, Andrew Menendez¹, Pedro Frigola³, Sergey Kutsaev³, Aurora Araujo³, Nanda Gopal Matavalam³, Prahalada Rao^{1,2*}

¹Mechanical and Materials Engineering, University of Nebraska-Lincoln, Lincoln, NE, USA ²Grado Department of Industrial and Systems Engineering, Virginia Tech, VA, USA ³Radiabeam Technologies, Santa Monica, CA, USA

*corresponding author: <u>prahalad@vt.edu</u>

Abstract

In this paper, we present the first known experimental results in using hybrid additive-subtractive laser powder bed fusion (h-LPBF) to make a type of passive radio frequency component called a quarter-wave resonator (QWR). The h-LPBF process uses in-situ, interlayer vertical milling to machine certain inaccessible, critical internal features of the QWR device during printing. Using h-LPBF, the as-built surface roughness of functionally important features improved to Ra ~ 2 µm compared to Ra ~ 8 to 20 µm for conventional (additive only) LPBF-processed QWRs. Additionally, the dimensions of certain critical features were closer to their intended design. These metrological improvements resulting from h-LPBF reduced RF losses by a factor of almost 2. Consequently, the RF performance of h-LPBF processed QWR components was 1.5 to 2 times superior compared to their conventional LPBF counterparts, and the performance advantage was sustained on stress relief and chemical etching. These results were verified with theoretical electromagnetic simulations.

Keywords: hybrid laser powder bed fusion (h-LPBF); quarter wave cavity resonator (QWR); surface finish; geometry; quality factor; resonant frequency.

1 Introduction

1.1 Hybrid Laser Powder Bed Fusion (h-LPBF)

Laser powder bed fusion (LPBF) is an additive manufacturing process, in which layers of metal powder are deposited on a substrate with a recoater blade or roller, and selectively fused using energy from a laser. Figure 1(left) shows a schematic of the LPBF process [1]. Commercial LPBF systems are equipped with an infrared fiber laser (250 – 1000 W) which is focused on the build plate using a f- θ lens. The desired profile is scanned by reflecting the laser beam with a pair of galvanometric mirrors (scanning speed 1 m·s⁻¹) [1].

The LPBF process enables the manufacturing of complex features that are difficult, if not impossible, to make using conventional subtractive and formative manufacturing, however, the parts tend to have poor surface finish relative to subtractive machining. Typically, the surface finish of as-built LPBF parts exceeds Ra $\sim 10~\mu m$ [2–4]. Likewise, the geometry and dimensions of the printed part deviates as much as \pm 150 μm from the nominal design due to thermal-induced deformation [5].

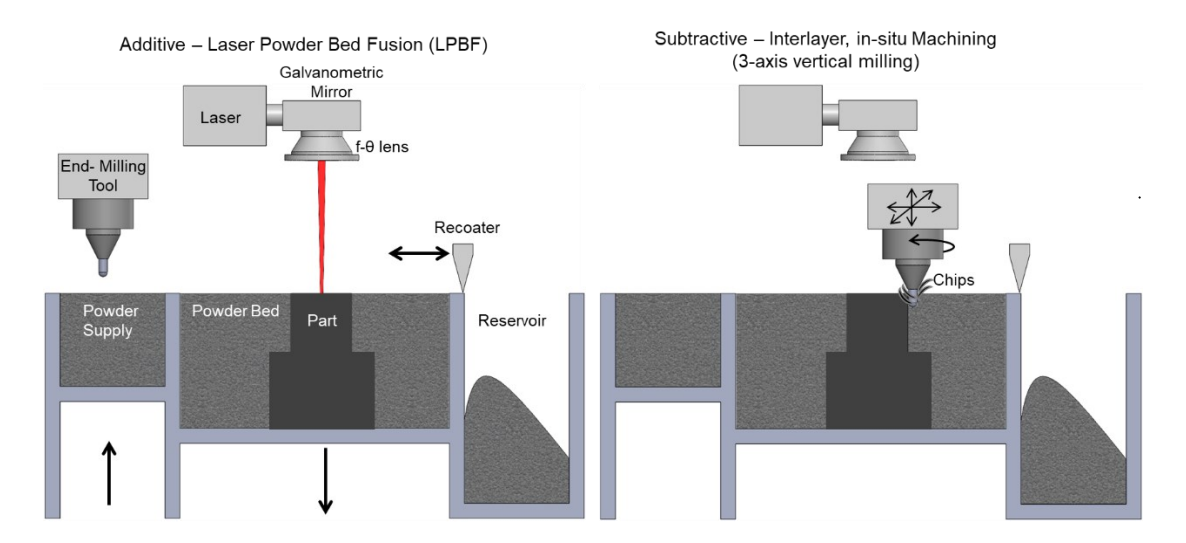


Figure 1: Schematics of (left) laser powder bed fusion (LPBF), and (right) hybrid additive-subtractive LPBF (h-LPBF) with in-situ, interlayer machining (vertical milling).

Therefore, for precision engineering applications, which require both tight dimensional and surface finish tolerances, LPBF parts are often machined or finished using post-processing [6,7]. A particular challenge is the finishing of complex and inaccessible geometries, such as internal non-cylindrical cooling channels and undercut surfaces. While superfinishing operations, such as magnetic rheological finishing, chemical machining, abrasive flow finishing, etc., can be employed for such purposes, the material removal rates of these processes tend to be slow, and controlled material removal from certain delicate surfaces is intractable [8]. Furthermore, the material removal in superfinishing tends to be anisotropic, thus resulting in a loss of geometric accuracy, which in turn impacts the functional integrity of the part [9].

A potential solution to overcome both the poor surface finish and degradation in dimensional accuracy of as-printed LPBF parts is to combine the process with an in-situ machining operation [10,11]. As shown in Figure 1(right), the key idea is to employ 3-axis vertical milling to remove material after a few layers have been additively processed (printed). This tandem, interlayer *hybrid* additive-subtractive LPBF operation is termed h-LPBF [10,11].

In h-LPBF, after a number of layers are fused, material in prior layers is machined using a vertical 3-axis milling operation. The machining interval is user-programmed and carried out typically after deposition of 10 layers (0. 5 mm). Material is removed in multiple passes, including roughing, semi-finishing and finishing passes. Commercial h-LPBF machines are equipped with an automatic tool changer with capacity of up to 40 cutting tools [10,11]. Typically, a ball end milling cutter ($\sim \Phi 2$ mm) is employed at spindle speeds approaching 30,000 RPM, with a feed rate of 1500 mm·min⁻¹. Under these machining conditions, the material removed per revolution of the milling tool is of the order of 50 μ m (10 to 25 μ m per tooth of the milling cutter). Hence, the size of the chips roughly matches the size of the LPBF powder feedstock and therefore does not impede

the deposition of succeeding layers. The high-speed and low chip load of the machining step results in surface roughness approaching the micrometer range and enables processing of delicate and complex features to tight tolerances.

An example of the metrological advantages accrued on h-LPBF is exemplified in Figure 2, which compares two h-LPBF and conventional LPBF processed parts. There is a pronounced improvement in the surface finish, as well as resolution of h-LPBF processed components (note the undercut in the N-shaped part). A limitation with h-LPBF is in the processing of surfaces in previous layers which have steep undercuts along the vertical (build) direction, as such surfaces would be inaccessible to the 3-axis vertical milling cutting tool.

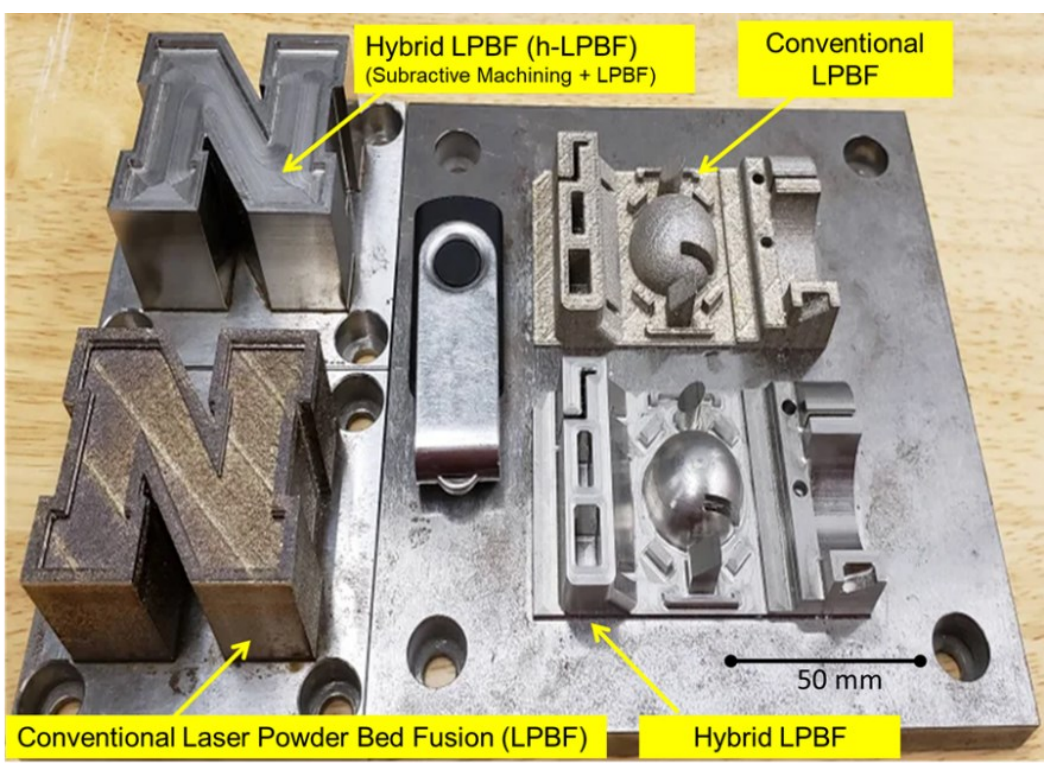


Figure 2: Example artifacts comparing the surface finish and resolution of conventional and hybrid-LPBF processes. These parts were printed on a Matsuura Lumex Avance 25 h-LPBF machine; the same machine is used in this work.

1.2 Objective and Novelty

The objective of this work is to use the h-LPBF process for the manufacture of a specific type of passive radio frequency (RF) component called the Quarter Wave Resonator (QWR). The h-LPBF process is distinct from hybrid additive-subtractive directed energy deposition (h-DED), which is well documented in the literature [12]. In comparison, there are relatively few published papers on h-LPBF [11,13–15]. Although the advantages of h-LPBF have been demonstrated in these prior publications, these studies concern simple-shaped parts (mainly maraging steel) that were not designed for a specific functional purpose. To the best of the authors' knowledge, this is the first published work to experimentally demonstrate application of h-LPBF for the production of complex, functionally-relevant and application specific RF components [10,11,13–15].

Additively manufactured RF devices have been investigated for applications in particle accelerators [16,17], quantum computing [18], nuclear fusion [19,20] and space-based telecommunications [21,22]. The QWR device studied in this work resonantly stores electromagnetic energy at a designed frequency, forming the basis for many band-pass filter devices. QWR devices are intricate, high-value components that are integral to a variety of applications ranging from radar equipment, satellite communication to high-energy particle physics [23]. Given their design complexity, particularly, presence of intricate internal features, QWRs are currently assembled from multiple components, hence, LPBF is potentially the process of choice to reduce manufacturing complexity, cost, and time-to-market.

The aim of this work is to improve the RF performance of QWRs through enhanced geometric accuracy and surface finish of selected surfaces afforded by h-LPBF. The typical average surface roughness (Ra) obtained for an as-built LPBF part is in the range of 10-20 µm, depending on the processing conditions, material, and part shape [2,3,24]. As a result, the as-printed QWR device

experience significant RF loss enhancement due to certain surface texture-related phenomena (as will be explained in depth in Sec. 2.1.2).

In this work, we demonstrate that using the h-LPBF approach significantly enhances the asbuilt surface finish of certain features critical to the functional integrity of QWR devices. The surface finish of such features improves to Ra \sim 2 to 3 μ m compared to those QWR devices produced with only LPBF whose surface finishes ranges from Ra \sim 6 μ m to 25 μ m. Additionally, the dimensions of the h-LPBF processed QWRs was closer to their design. In other words, h-LPBF affords significant improvement in surface finish without sacrificing dimensional accuracy. Consequently, the functional performance (Q-factor) of h-LPBF processed QWRs improves by a factor of 1.5 to 2 over their conventional LPBF-processed counterparts. Moreover, the performance improvement afforded by h-LPBF was sustained through post-processing (stress relief and chemical etching).

The rest of this paper is structured as follows. In Sec. 2, we detail the methodology, encompassing the QWR design; theoretical insights into how and why surface finish and geometric integrity impact the RF performance based on simulation of the electromagnetic field; h-LPBF process methodology; post-process finishing steps (stress relief and chemical etching); post-process characterization of physical properties (surface finish, dimensional integrity, microhardness, and electrical conductivity); and measurement of RF performance. The results are reported in Sec. 3, wherein the RF performance improvement of QWR devices accrued due to h-LPBF is compared with their conventional LPBF processed counterparts. Finally, conclusions and avenues for future work are identified in Sec. 4.

2 Methodology

2.1 Test artifact

2.1.1 Background - Quarter Wave RF Cavity Resonator (QWR)

The geometry of the QWR component studied in this work is shown in Figure 3. The rationale for the design and RF characteristics of this QWR device is discussed in detail in Ref. [25]. Noting that the electromagnetic energy is contained entirely within the internal volume of the cavity of the device, the three internal surfaces of the QWR most consequential to its RF performance are demarcated in Figure 3(a): (i): the outer conductor (OC, purple); (ii) center pin (CP, red), also called inner conductor; and (iii) shorting plate (SP, blue). Additional test surfaces (TS, green) are distributed around the outer circumference of the QWR. Each of the six test surfaces (TS) is tilted at a different angle to the horizontal ranging from 20° to 70° in steps of 10°. These external test surfaces are inconsequential to the RF performance, and act as references for qualifying surface finish and geometric integrity.

Practically, the QWR design for this work is small, short and low-cost from a LPBF perspective. Additionally, it can be directly scaled to operate at different frequencies by changing the length of the center pin; contains non-trivial and complex geometries to demonstrate the practical advantages of h-LPBF; and can be oriented in different build directions for manufacturability. More pertinently, two aspects of RF performance metrics: (i) the resonant frequency (f₀), and (ii) the quality factor (Q) can be measured precisely for this device, which in turn provides an understanding of the effect of geometric accuracy and surface finish losses on the functionality of the device. While a variety of metal powders, e.g., titanium, steel, nickel, cobalt and copper alloys, can be used, AlSi10Mg alloy was chosen for the relatively high electrical conductivity, reliable suppliers with good material quality, and well understood AM process maps

[26,27]. In the following section (Sec. 2.1.2) we provide a brief theoretical background on how and why the surface finish of the QWR device influences its functional RF performance.

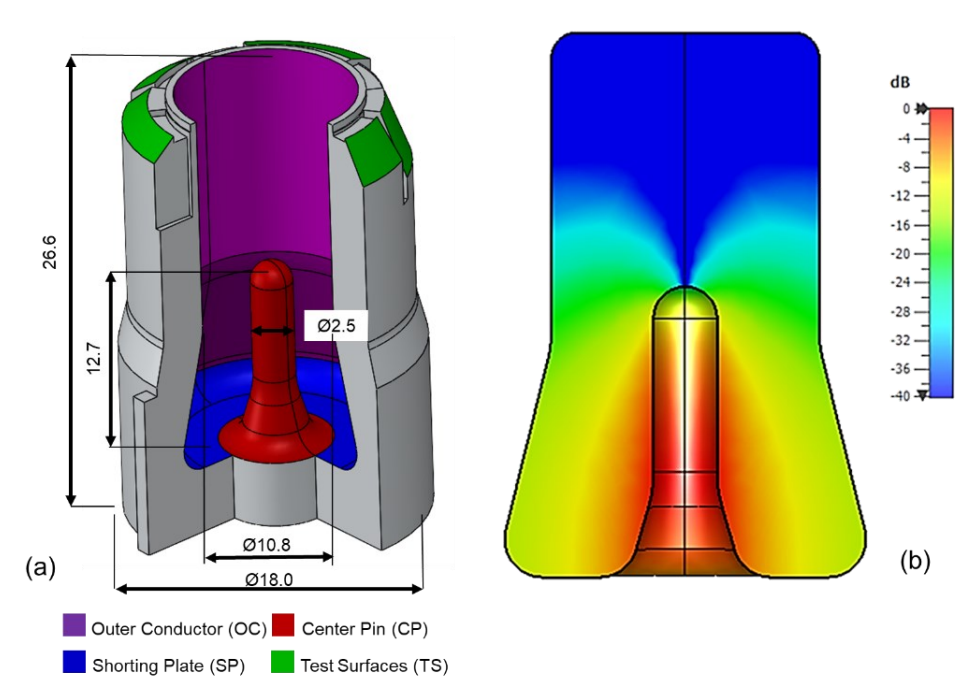


Figure 3: (a) The quarter wave resonator (QWR) used in this work. A quadrant has been cut away for interior clarity. The three internal features of the part in descending order of importance: the red center pin (CP), blue shorting plate (SP), and purple outer conductor (OC). The green external test surfaces (TS) have no impact on RF performance and are for surface texture reference measurements. (b) COMSOL simulation of the magnetic field distribution in logarithmic scale, showing that 65% of the electromagnetic energy is concentrated around the center pin (CP). Hence the physical characteristics (surface finish and geometry) of the CP is crucial to the functional performance of the QWR [25]. All dimensions shown are in millimeters.

2.1.2 Effect of Surface Finish and Geometric Integrity on RF performance

(a) Effect of Surface Finish

Coupon-level studies performed on LPBF-processed RF surfaces reveal that the electrical performance is hampered by the power losses associated with the characteristic rough surface of internal features [28,29]. The surface has a consequential effect on the RF performance of the QWR in normal-conducting state due to a phenomenon called the *skin effect*, whereby the majority of current in the RF device is contained within a skin depth $(\delta) \sim 1 \mu m$.

The relationship between the operating frequency f, material properties, and skin depth (δ) is given by,

$$\delta = \sqrt{\frac{1}{\pi f \mu \sigma}} \tag{1}$$

where f is the operating frequency [Hz], μ is magnetic permeability [H·m⁻¹] and σ is the bulk electrical conductivity [S·m⁻¹]. With the nominal material properties in the context of the AlSi10Mg QWR device of this work: f = 6 GHz, $\sigma = 26.1 \times 10^6$ S·m⁻¹, and $\mu = 1.256 \times 10^6$ H·m⁻¹, we estimate the skin depth, $\delta \approx 1.2$ μ m.

The RF power dissipation of an ideal, smooth surface is defined by the surface resistance, R_{s0} [Ω], which is a function of both skin depth and conductivity:

$$R_{s0} = \sqrt{\frac{\pi f \mu}{\sigma}} = \frac{1}{\delta \sigma} \tag{2}$$

For the previous nominal parameters used in Eqn. (1), the ideal $R_{s0} = 30$ m Ω . Practical subtractive manufacturing tolerances require critical RF surfaces to have a roughness $Ra \le \delta$. Rough surfaces, which are defined by $Ra >> \delta$, increase the developed interfacial surface area and thus increase the RF losses. A simple empirical relationship that captures the surface resistance enhancement is $R_s = \eta R_{s0}$, where η is the *loss enhancement factor*, $\eta > 1$.

While it is difficult to capture the impact of various scales and forms of surface texture on RF performance within an analytical model [30], the Hammerstad model, which assumes a regular triangular grooved surface typically observed in subtractive machined parts, is often used to approximate η [31]. Characterizing LPBF surface texture is a particularly challenging proposition, since the surface texture depends on processing parameters (scan pattern, laser power, velocity),

part orientation and measurement method [2,3]. Furthermore, the characteristic stair-step surface texture of LPBF parts coupled with the effect of near-surface fused powder severely limits the use of conventional surface metrology [32].

(b) Effect of Part Geometry

The QWR center pin length, L, corresponds to a quarter of the resonant wavelength ($\lambda_o/4$). To a first approximation, the resonant frequency for the QWR shown in Figure 3 is $f_0 = c/\lambda_o = c/4L = 5901.42$ MHz, c is the speed of light. The logarithmic peak magnetic field distribution is shown in Figure 3(b). These magnetic fields were obtained from a computational simulation of the QWR device (COMSOL eigenmode RF simulation). The simulation confirms that the resonant frequency of the QWR device corresponds to $f_0 = 6014.20$ MHz (termed C-band according to IEEE nomenclature). The deviation between the analytical and computed f_0 is due to secondary features: hemispherical center pin termination, center pin and taper of the outer conductor.

RF losses are captured by the quality factor, Q, which is a dimensionless parameter that describes the oscillator dampening. High-Q devices indicate reduced power loss rate, i.e., the RF oscillations decay slowly. Mathematically, the Q-factor is the energy stored in the cavity volume divided by the energy dissipated along the cavity surfaces. Assuming only eddy current losses, Q is defined according to [33],

$$Q = 2\pi f \mu_0 \frac{\iiint |H|^2 dV}{\iint |H|_{V}^2 dA} = \frac{G}{R_s}$$
 (3)

where μ_0 is the permeability of free space, the numerator integral is the magnetic energy stored in the cavity volume; the denominator integral represents the eddy current induced fields along cavity surface. The quotient of the two integrals can be simplified to $Q = G/R_s$, where $G[\Omega]$ is a frequency-independent *geometry factor* and R_s is the previously defined RF surface resistance.

From COMSOL simulations, the geometry factor for the QWR in this work is computed to be G = 71.5 Ω . Using the previously defined nominal RF parameters ($R_{s0} = 30 \text{ m}\Omega$), the ideal Q-factor of the QWR is Q = 71.5 Ω /30 m Ω = 2383. Alternatively, if the RF surface resistance (R_s) increases due to surface texture effects, we expect Q = G/(η R_{s0}), where η >1.

Further examining the magnetic fields of Figure 3(b), we note that the fields are largely concentrated around the center pin (CP), implying the large weighted effect of the center pin on the quality factor. Mathematically, we can capture this geometry effect by examining the reciprocal of Q,

$$\frac{1}{Q} = \frac{\iint |H| \langle dA| dA}{2\pi f \mu_0 \iiint |H|^2 dV} \tag{4}$$

which represents the ratio of energy dissipated in the walls to the energy stored in the volume of the QWR. Furthermore, we can partition the surface integral according to the center pin (CP), shorting plate (SP) and outer conductor (OC) surfaces defined in Figure 3(a),

$$\frac{1}{Q} = \frac{\iint |H|_{\backslash \backslash}^2 dA_{CP} + \iint |H|_{\backslash \backslash}^2 dA_{SP} + \iint |H|_{\backslash \backslash}^2 dA_{OC}}{\omega \mu \iiint |H|^2 dV}$$
(5)

from Eqn. (5) we define the G and R_s for each relevant surface according to,

$$\frac{1}{Q} = \frac{R_{s-CP}}{G_{CP}} + \frac{R_{s-SP}}{G_{SP}} + \frac{R_{s-OC}}{G_{OC}} = \frac{1}{Q_{CP}} + \frac{1}{Q_{SP}} + \frac{1}{Q_{OC}}$$
(6)

In other words, the Q-factor of each surface act akin to parallel resistors. The motivation for this definition is important for LPBF-processed components, as they encompass vertical surfaces for the center pin (CP), horizontal surfaces for the shorting plate (SP), and overhanging surfaces for the outer conductor (OC), noting each feature has its own loss enhancement factor η_i . The geometry factor G for each feature is predicted from COMSOL as, $G_{cp} = 111 \Omega$; $G_{sp} = 346 \Omega$; $G_{oc} = 482 \Omega$.

Substituting these values into Eqn. (6) yields:

$$Q = \frac{1000}{9R_{s-CP} + 2.9R_{s-SP} + 2.07R_{s-OC}}$$
 (7)

From Eqn. (7) we see that, the effective RF surface resistance of the center pin, R_{s-CP} , has the most significant impact on the Q-factor.

2.2 Experiments

The QWR parts were created on a Matsuura Lumex Avance 25 hybrid-LPBF system [34]. The AlSi10Mg powder (TEKMAT AlSi10Mg-63/20) used in this work had the following distribution: $D_{10} = 26 \mu m$; $D_{50} = 41 \mu m$; $D_{90} = 61 \mu m$. The processing parameters used in this work are summarized in Table 1. These parameters are based on recommendations of the machine tool manufacturer (Matsuura) and were obtained through empirical optimization. The build plate consisting of six QWR devices and other geometries is presented in Figure 4. The six QWR devices created in this work are labeled S1, S2, S3, M1, M2, and M3. The other geometries on the build plate are design-of-experiments density cubes which are outside of the scope of this work.

Each of the QWR devices in this work consist of 625 layers and the process was completed in 16 hours. Three QWRs labeled S1, S2, and S3 were processed with only LPBF; QWRs labeled M1, M2, and M3 were processed with h-LPBF. In the h-LPBF step, machining was conducted on four surfaces identified in Figure 3(a), viz., CP, SP, OC, TS. The QWR labeled M1 received machining only on the center pin (CP) surface; M2 received machining on central pin (CP) and shorting plate (SP), and M3 received machining on the CP, SP, OC and the outer test surfaces (TS). For M3, it was not possible to machine the entire length of the outer conductor (OC) during h-LPBF due to the overhang and undercut features near the bottom. As a result, in this work, the effect of machining the outer conductor would be negligible to the RF performance of the QWR.

However, machining the outer conductor provides a critical benchmark for assessing the surface finish for internal features resulting from h-LPBF. In h-LPBF, an extra 250 μ m of stock (machining allowance) was added to these machined surfaces in the slicing software. Material was removed after every 10 layers of deposition (0.5 mm) in three passes: roughing pass (130 μ m of material removed), semi-finishing (90 μ m), and finishing (30 μ m). The machining parameters for the h-LPBF process are detailed in Table 1.

The QWR devices were placed on the far side of the build plate, perpendicular to the recoater and gas travel direction along the x-axis. No parts are placed in front or behind the QWRs, and they were always processed before the other parts on the build plate. This was done for the following three reasons: prevent build failures of one resonator from affecting other components; ensure consistent gas flow across all resonators, thus reducing the effect of location on the part quality; and facilitate the removal of spatter particles by the gas flow.

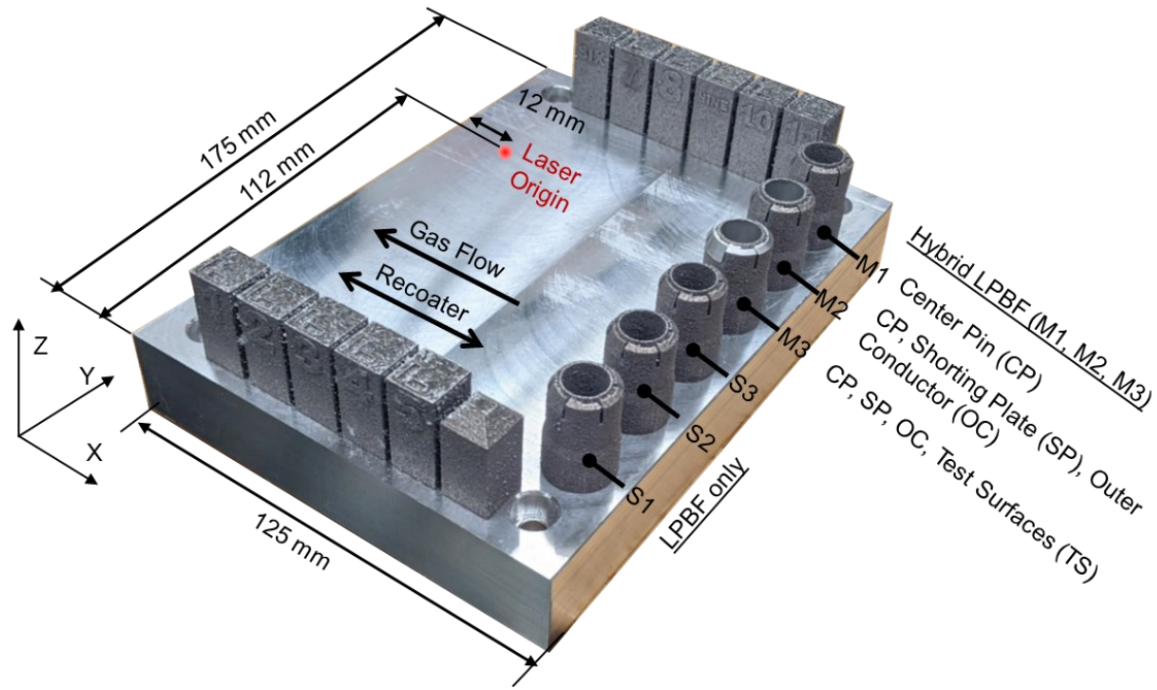


Figure 4: Completed build plate. Six resonators were created in this work. Three resonators labeled M1, M2 and M3 were hybrid machined on various surfaces labeled CP, SP, OC, TS. Three parts labeled S1-S3 were made using conventional LPBF.

As an aside, the chips from the machining process were examined. The chips were observed to be of the continuous type with typical length exceeding 1 mm. Consequently, the chips are readily removed by sieving the powder before reuse. We note that in this work, we used fresh, unused powder.

Table 1: Summary of materials and processing parameters.

Process Parameter	Values [units]		
Laser type and wavelength.	1070 nm continuous wave		
Laser power (P) [W]	360		
Scanning Speed (V) [mm·s ⁻¹]	600		
Hatch spacing (H) [mm]	0.27		
Layer thickness (T) [mm]	0.05		
Laser spot size	300 μm with top hat power distribution		
Scanning strategy	Island Scanning Strategy		
Build atmosphere	Nitrogen		
Build plate Preheat temperature [°C]	50° C		
Material Properties	Values [units]		
Material type	TEKMAT™ AlSi10Mg-63/20		
Particle size [µm]	$D_{10} = 26$; $D_{50} = 41$; $D_{90} = 61$		
Machining Parameters	Values [units]		
Removal allowance [µm]	250		
Machining Sequence	1. Roughing: 130 μ m, Φ =2.0 mm ball mill.		
depth of cut,	2. Semi-finishing: 90 μ m, Φ =2.0 mm ball mill.		
dia. (Φ) tool used	3. Finishing = 30 μ m; tool shank Φ = 1.8 mm ball mill		
Tooling:	Two flute carbide ball end mills.		
Machining parameters	1. Roughing: 2000 mm/min, 30,000RPM		
Feed rate, RPM.	2. Semi-finishing: 2000 mm/min, 30,000RPM		
	3. Finishing: 1600 mm/min, 37,000RPM		



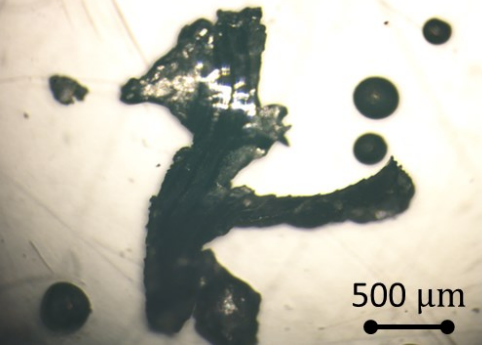


Figure 5: Chips from the h-LPBF process were of the continuous type exceeding 1 mm in length,, and are readily removed by sieving the powder prior to reuse.

2.3 Post-processing

After completion, each QWR was removed from the build plate via electro-discharge machining, and excess powder was removed using isopropyl alcohol. To improve physical properties, two post-process enhancements were implemented, namely, stress relief, followed by chemical etching.

The as-built QWRs were stress relieved in a nitrogen atmosphere at 300 °C for 2 hours. Heat treatment reduces the ideal RF surface resistance (R_{s0}), but does not impact the surface roughness, i.e., the surface enhancement factor η remains unchanged. This is because, as elucidated by Silbernagel *et al.* [35], the process of stress relieving changes the material structure of AlSiMg10, which in turn effects the resistivity.

After stress relief, the parts were chemically etched in hydrofluoric acid (HF) for 30 seconds followed by a 5 second etch in a 1:3 HF:HNO₃ mixture per the ASTM B253 – 11(2017) *Standard guide for preparation of Aluminum alloys for electroplating*. In contrast to stress relief, the chemical etching process reduces the roughness enhancement factor η (improves surface finish) but does not change the surface resistance (R_{s0}).

2.4 Part characterization

2.4.1 Dimensional Metrology and Density

The dimensional integrity of as-built QWRs was assessed using X-Ray computed tomography (X-ray CT, Nikon XTH225) at a voxel resolution of 15 µm, enabling detection of feature deviations as small as 30 µm [36]. For this purpose, a nominal/actual comparison (NAC) analysis is conducted over the entire volume of the as-built QWRs design using the Volume Graphics (VGSTUDIO MAX) software native to the XCT machine. The analysis involves comparing dimensions of the as-built QWRs to their ideal CAD model, and results in a 3D deviation map.

Additionally, X-ray CT analysis was conducted to ascertain the as-built density of the QWRs in terms of percentage defect volume ratio (DVR).

2.4.2 Surface Metrology

Surface texture measurements on the machined surfaces was performed with a calibrated contact profilometer (Mitutoyo SJ-410). The surface profile measurements were obtained using a 2 μ m tip radius at a speed of 0.51 mm·s⁻¹ with 5 repeats per measurement. The hardware applied a Gaussian filter to the data with, $\lambda c = 0.03$ mm, $\lambda s = 2.54$ mm. Due to the rough texture of the asbuilt LPBF parts, accurate profilometer measurements of the as-printed external test surfaces (TS, Figure 3(a)) were not possible. Consequently, the surface roughness of the external test surfaces (TS) was measured using a depth-of-focus variation optical surface profiler (Keyence VHX-6000).

2.4.3 Microhardness and Electrical Conductivity

Vickers Microhardness measurements (Micromet II) were obtained by making indents on the base of the QWR devices in accordance with ASTM E92-17. Periodic verification was performed against a standard test block (Wilson hardness test block 168HV1/15). Microhardness readings were acquired in two stages: as-built and after stress relief. Surface electrical conductivity measurements were obtained using a Eddy Current probe operating at 480 kHz (SigmaScope SMP10) in accordance with ASTM E1004 with periodic calibration against an annealed oxygen free copper sample certified to 101% IACS.

2.5 RF Measurements

Three rounds of RF measurements were conducted for each QWR device to measure the resonant frequency (f_0) and quality factor (Q). These RF measurements were conducted after the following stages: (i) as-built; (ii) after stress-relief; and (iii) after chemical etching.

RF performance was measured in S11 using a network analyzer (Agilent F8362B). Open, short and load calibration was performed using an Agilent N4433A Electronic Calibration Module. For RF measurements, samples were clamped onto an RF test fixture shown in Figure 6(a) with silver plated contact surfaces. The electric field coupling was manually adjusted by trimming a copper pin extending into the cavity, as shown in red of Figure 6(b), with an average penetration of 3.2 mm and coupling coefficient estimated to be $\beta \approx 0.1$ to 0.2. The coupling coefficient unloaded quality factor was numerically calculated in MATLAB using a standard fitting routine established in the literature [37].

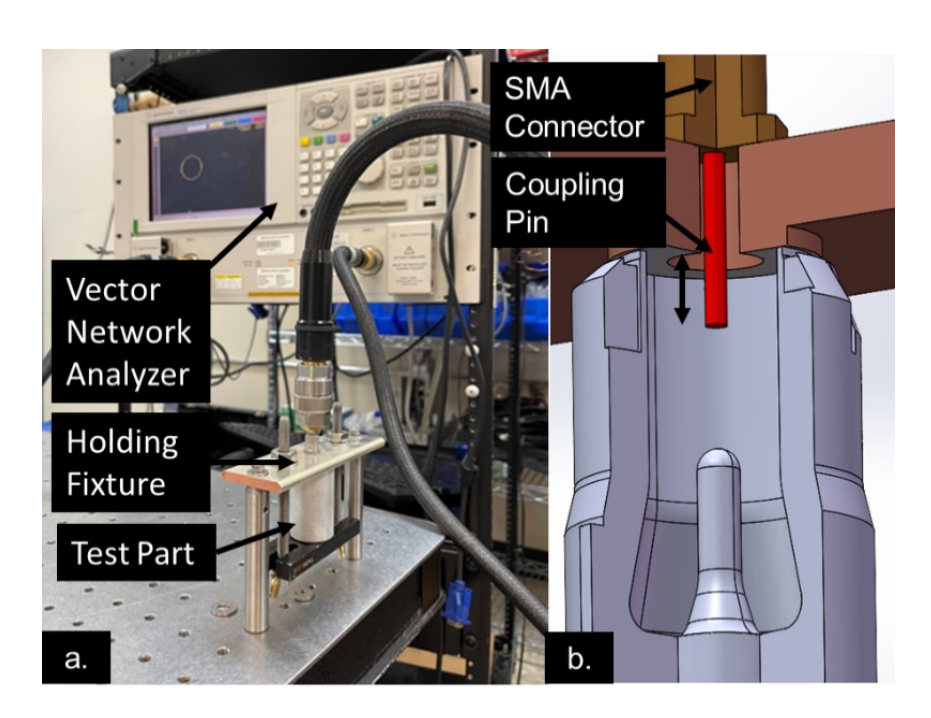


Figure 6: (a) CAD Model of the S11 RF fixture setup showing the variable coupling RF probe. (b) RF fixture setup for measurement.

3 Results and Discussion

3.1 Surface Finish

Surface quality was significantly improved by h-LPBF as visually evident in Figure 7. Shown in Figure 7 are top views of as-built S3 and M3 QWRs with emphasis on the test surfaces (TS), and center pin (CP). The geometric resolution and surface finish of as-built LPBF processed QWRs, and additively manufactured parts in general, is limited by the layer height (50 µm), which in turn causes a characteristic stair stepping effect when there is a change in the part cross-section in the vertical direction. The stair stepping effect is particularly prominent in the hemispherical-shaped tip of the center pin (CP) of the LPBF-processed QWR device S3.

The surface roughness measurements of the six external test surfaces (TS) and outer conductor (OC) are shown in Figure 8. For the LPBF produced resonator S3, the surface roughness (Ra) for the TS was in the range of 6 μ m to 25 μ m. By contrast, the surface roughness of the h-LPBF processed QWR device M3 was in the range of 2 μ m to 3 μ m. The surface roughness measurements obtained on the outer conductor (OC) were as follows. For the LPBF processed QWR S3: Ra = 8 ± 1 μ m, with peak and valley heights of Rp = 16 ± 2 μ m, and Rv = 17 ± 1 μ m; for the h-LPBF processed QWR M3: Ra = 2 ± 1 μ m, Rp = 4 ± 1 μ m, and Rv = 6 ± 1 μ m.

We note that these surface finish measurements in Figure 8 are from 5 independent replications; the surface finish measurements were made normal to the surface form. The observed surface finish variation is therefore intrinsic to the surface of each part and not due to instrument error. Moreover, the large magnitude, as well as variation in surface finish of as-built LPBF parts S1-S3 presented in Figure 8, is consistent with the literature. For example, Subramanian *et al.* [38], observed that the surface finish of LPBF parts is contingent on the incident angle of the laser and the build orientation. Subramanian *et al.* [38], report that the surface finish of inclined features,

such as the test surface (TS) of the QWR, may vary as much as Ra \sim 6 to 8 μ m, because the laser incidence angle changes continually during melting of overhang features. In contrast, the variation in surface finish for vertical surfaces, e.g., outer conductor (OC), is restricted to less than 1 μ m, as the incident angle of the laser beam does not change considerably.

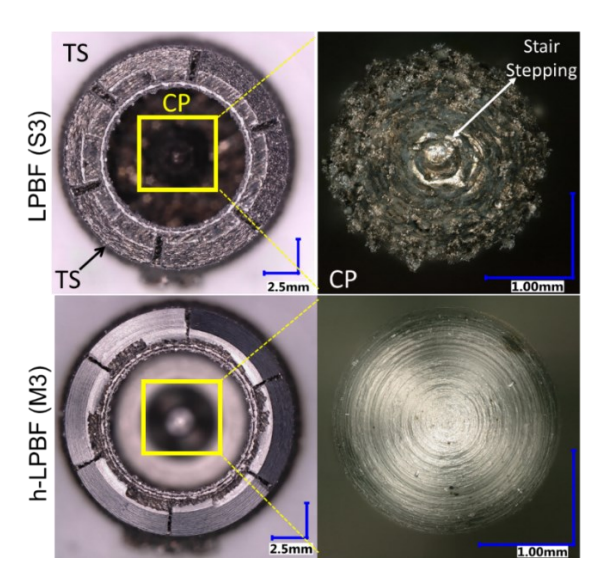


Figure 7: Optical microscopy images of an as-printed and hybrid machined resonator center pins. The as-printed resonator pins (top row) show a high surface roughness and layer based "stair stepping". The hybrid-additive pin (bottom row) has a lower surface roughness, and the pin shape is much closer to the intended design.

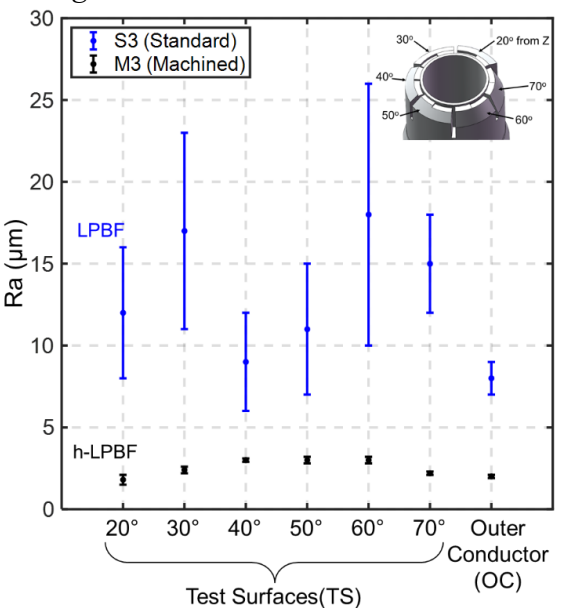


Figure 8: Surface roughness of outer test surfaces for the S3 (conventional LPBF) and M3 (h-LPBF) quarter wave resonators.

3.2 Dimensional Integrity and Density

The X-ray CT analysis further highlights the dimensional accuracy improvement with h-LPBF. Presented in Figure 8(top) are the nominal/actual comparison (NAC) results for the LPBF processed QWR device S1, and h-LPBF processed QWRs, M1, M2, and M3. If the actual dimension of the as-built QWR device is larger than nominal CAD model, the feature is assigned a positive deviation with a yellow to red hue. Likewise, if an actual feature has dimensions smaller than its nominal, it is designated as a negative deviation with a blue hue. An ideal match between nominal and actual results in a green color.

Comparing the deviation map across only LPBF-processed QWR (S3), and h-LPBF processed QWR devices (M1, M2 and M3), it is evident that the h-LPBF processed components adhere closer to design dimensions. For example, comparing the center pin (CP) of S1 with its h-LPBF counterparts M1, M2 and M3, it is apparent that the center pin of S1 has a negative deviation approaching 100 µm, while those of the h-LPBF resonators is closer to the nominal design.

In a similar vein, Figure 9 (middle row) compares a 2D longitudinal X-ray CT cross-section of LPBF and h-LPBF resonators. The machined surfaces (denoted with yellow triangles) show a reduced surface roughness. From these 2D cross sections, a limitation in the h-LPBF tool path planning software algorithms (MasterCAM) was identified: the periphery of the shorting plate (SP) was left unmachined. The tool path planning software includes a tool-crash recognition algorithm; the software automatically determined that the milling tool would not have access to the area under the taper of the outer conductor. While this would be true for conventional subtractive processes, the taper was not yet printed thus making tool crashes impossible. This exposes a limitation of using commercial off-the-shelf tool path planning software for h-LPBF.

Despite this limitation, the X-ray CT results show that there is a pronounced improvement in overall geometric accuracy, as well as surface finish of the interior features of the h-LPBF processed resonators, particularly with respect to the two most critical features, i.e., center pin (CP) and shorting plate (SP). As shown in the succeeding section, Sec. 3.4, the improvement in dimensional integrity and surface roughness resulted in a significant improvement in RF performance. The marked difference in surface finish and texture on h-LPBF is evident on examining the top view of the QWR devices presented in Figure 9.

Lastly, X-ray CT analysis revealed that the defect volume of ratio (DVR) of the QWRs was in the range of 0.06 to 0.30% (Table 2) implying that the density of the as-built parts exceed 99.7%. The density of the h-LPBF processed QWRs is comparatively lesser that the LPBF counterparts, this are likely a result of machining marks, that are erroneously detected as voids by the Volume Graphics (VGSTUDIO MAX) software native to the X-ray CT machine.

Table 2: Density measurements from X-ray CT in terms of the Defect volume ratio (DVR). The density of the as-built QWR exceeds 99%.

Quarter Wave Resonator (QWR)		Defect Volume Ratio (DVR, [%])		
S1		0.11		
S2	LPBF only	0.07		
S3		0.06		
M1	h-LPBF, Center pin (CP)	0.24		
M2	h-LPBF, CP, Shorting plate (SP), outer	0.30		
	conductor (OC)			
M3	h-LPBF, CP, SP, OC, test surfaces (TS)	0.30		

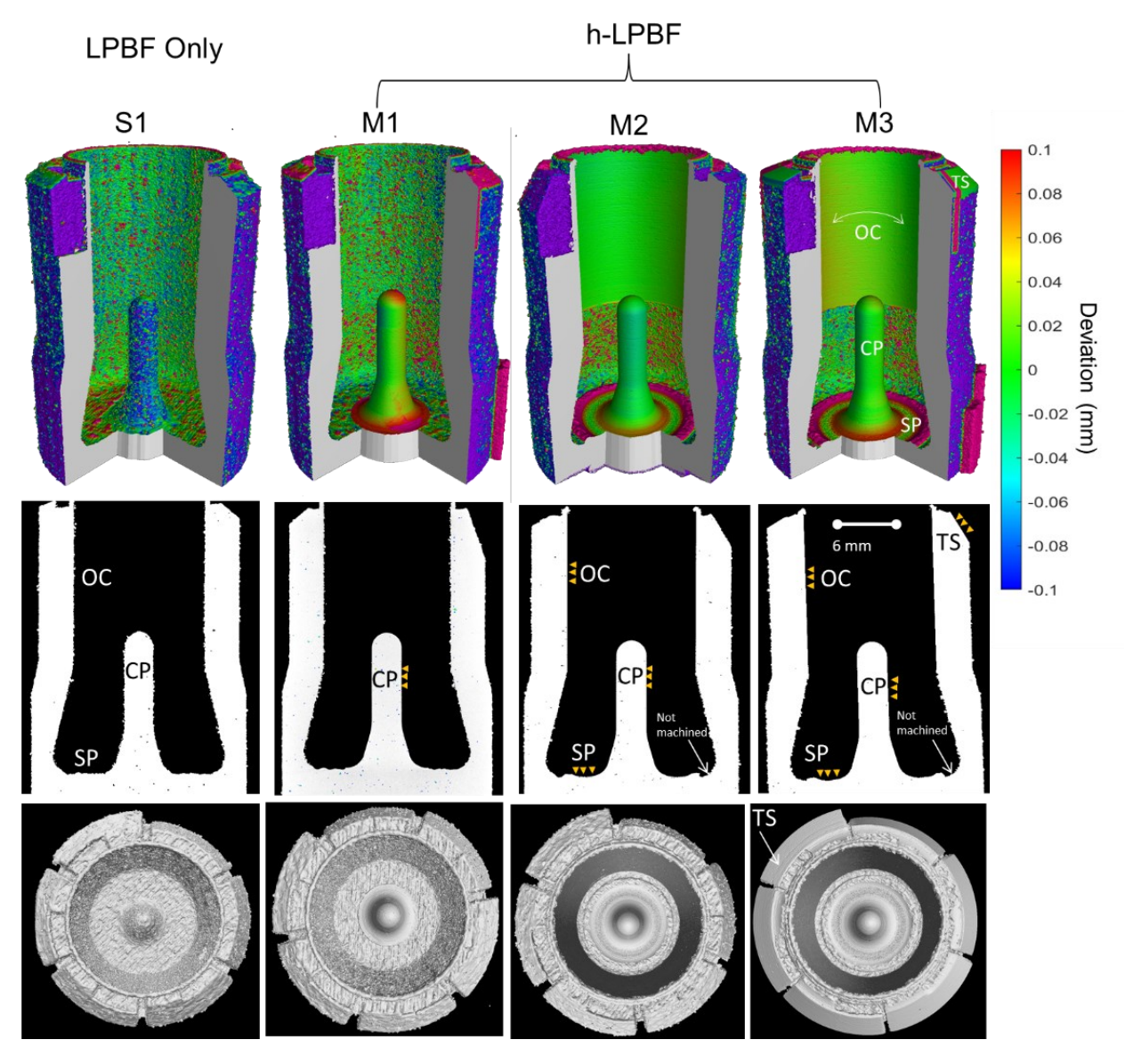


Figure 9: X-ray CT comparison of as-printed conventional LPBF resonator S1 and hybrid-LPBF resonators (M1, M2, and M3). (top) nominal/actual analysis, with surface deviation colored relative to the CAD model. The center pin of h-LPBF resonators has considerably less deviation compared to S1. (middle) vertical X-ray CT slice showing the improvement of surface finish of h-LPBF parts. (bottom) top view X-ray CT slice affirming the enhanced geometric integrity and surface finish of h-LPBF processed resonators compared to S1.

3.3 Microhardness and Surface Conductivity

Vickers hardness and surface electrical conductivity measurements were not significantly different for the LPBF and h-LPBF devices both in as-built and stress relieved conditions. However, as shown in Table 3, on stress relief the microhardness reduced while electrical conductivity increased substantially.

Table 3: Electrical conductivity and microhardness readings of resonators in the as-built and stress relieved states. All resonators had similar results, as such the results are bounded.

	As-built	Stress Relieved
Conductivity (%IACS)	23.2 ± 1%	45 ± 1%
Vickers Microhardness (HV1/15)	135 ± 5	80 ± 3

3.4 RF Performance

Figure 10 and Table 4 report the quality factor (Q) and resonant frequency (f₀) measurements for the QWR devices in 3 different states – as-built, after stress relief, and after chemical etching. As evident from Figure 10(a), the quality factor (Q) of h-LPBF processed QWR devices is nearly 1.5 to 2 times superior to their LPBF processed counterparts, and this performance advantage is sustained despite post-process stress relief and chemical etching,

In Table 4, these results are also compared with the ideal RF response from COMSOL simulations (Figure 3b), noting that the resonator was designed for a resonant frequency (f_0) of 6014 MHz, and the ideal quality factor (Q_0) was 1893 for as-built and 2367 for stress-relieved and chemically etched devices, respectively.

Further interpreting the detailed results reported in Table 4, as summarized in Figure 10(b), the as-built h-LPBF parts showed a marked improvement in functional integrity; the mean quality factor of as-printed h-LPBF resonators was measured at Q = 970 compared to Q = 484 for

conventional LPBF resonators. Moreover, the standard deviation of the quality factor for h-LPBF resonators was 25 units, compared to 233 units for the conventional LPBF processed resonators. Hence, using h-LPBF not only doubled the mean quality factor, but also improved the consistency of RF performance.

Stress relief increased the quality factor of all resonators by an average of 25% for both LPBF and h-LPBF processed resonators. The quality factor again increases across by another 25% on chemical etching the stress relieved h-LPBF resonators. The improvement in quality factor of stress relieved and chemically etched LPBF-processed QWRs over as-built devices was more pronounced (~80%) compared to h-LPBF as loose powder or exposed particles were potentially removed due to the superfinishing effect of chemical etching.

As observed in Table 4, the quality factor of h-LPBF resonators also improved subsequent to stress relief to Q = 1200, and after etching to Q = 1576 units. More pertinently, while the quality factor of conventional LPBF-processed resonators after stress relief increased to 600 units, and after chemical etching improved to 1055 units, these improvements are nevertheless only marginally better than that of as-built h-LPBF resonators (970).

In the context of the resonant frequency (f_0), both h-LPBF and conventional LPBF processed resonators were within 4% of the designed resonant frequency response of 6014 MHz, thus confirming that hybrid-LPBF does not deleteriously influence the desired frequency operating regime of the resonator. Indeed, as evident in Figure 10(a), the resonant frequency (f_0) of h-LPBF processed QWRs (mean f = 5986 to 5995 MHz) was closer to the ideal ($f_0 = 6014$ MHz) compared to LPBF processed QWRs (mean f = 5951 to 5972 MHz).

In other words, despite post-process stress relief and etching, the performance of conventional LPBF processed resonators is significantly inferior to their h-LPBF processed counterparts. This is because the improvement in interior surface roughness due to etching is marginal compared to the improvement resulting from the machining step in h-LPBF. For example, as depicted in Figure 8, the surface finish of the outer conductor (OC) of as-built conventional LPBF QWR part S3 is $Ra \sim 8~\mu m \pm 1~\mu m$, compared to $Ra = 2 \pm 1~\mu m$ for the h-LPBF processed part M3. To explain further, the etching process, which lasts for 35 seconds, results in material removal of $\sim 1~\mu m$, which is not sufficient to improve the surface finish to the degree afforded by h-LPBF. Instead, the etching process facilitates removal of loose powder partially fused to the surface, resulting in improvement in the quality factor. Consequently, the performance of conventional LPBF QWR parts do not supersede their h-LPBF counterparts after similar stress relief and etching.

Table 4: Summary of electrical performance characteristics under the as-printed, stress relieved(SR) and etched conditions. Hybrid machined resonators have a resonant frequency much closer to the intended design. Resonator quality factor is much improved and made more consistent by the hybrid machining process.

	Resonant Frequency Response f ₀ [MHz]			Quality Factor Q [A.U.]					
	As- printed	Stress Relieved	Stress Relieved and Etched	As-printed	Stress Relieved	Stress Relieved and Etched			
Hybrid LPBF (h-LPBF)									
M1 (CP)	5973	5962	5967	948	1186	1420			
M2 (CP, SP, OC)	6007	5996	5996	990	1219	1671			
M3 (CP+SP+OC+TS)	6006	5995	5996	974	1219	1638			
Mean	5995	5984	5986	970	1208	1576			
Standard Deviation	19.3	19.3	16.4	21.1	19.0	136			
Conventional LPBF (S1, S2, S3)									
Mean	5951	5941	5972	484	600	1055			
Standard Deviation	20.1	19.6	6.0	233.4	328.1	99.9			
	Theoretical Values (From COMSOL simulations)								
	$f_0 = 6014 \text{ MHz}$			Q = 1893	2367	2367			

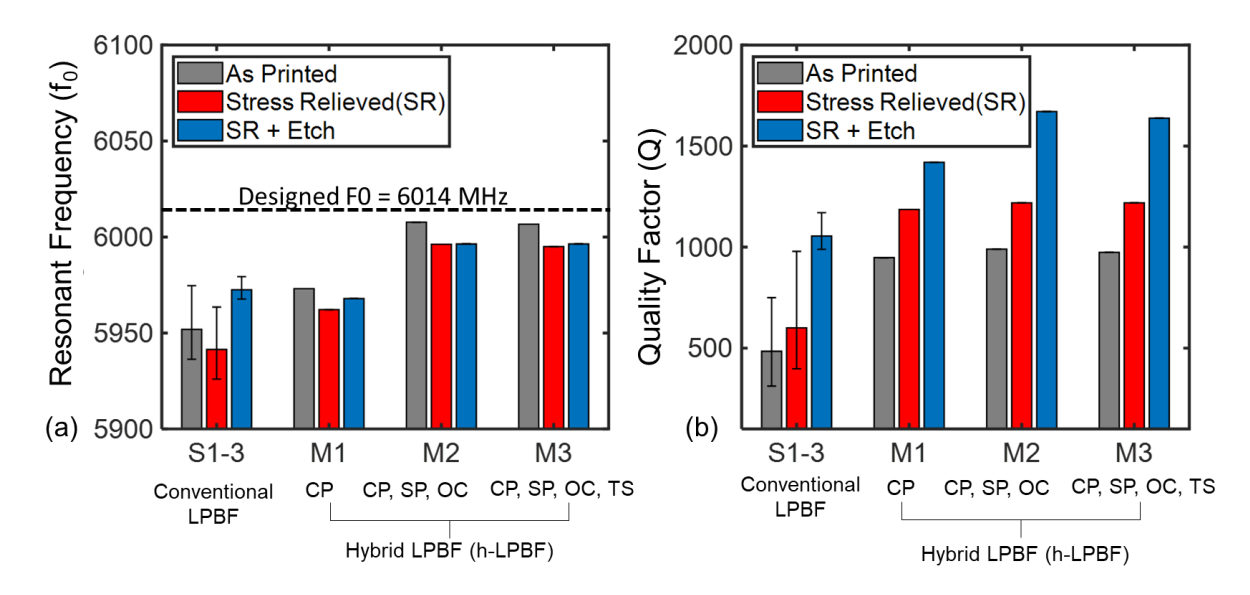


Figure 10: Comparisons of the (a) resonant frequency (f₀) and (b) quality factor (Q) of conventional LPBF-processed QWRs (S1,S2, and S3) and h-LPBF processed QWRs (M1, M2, and M3). Minimum and maximum results are presented as error bars for LPBF QWRs. Resonant frequency for the h-LPBF QWRs was much closer to the design intent than LPBF processed counterparts. Similarly, for the h-LPBF processed QWR parts the quality factor improved significantly and more consistent than the conventional parts.

4 Conclusions

In this work we accomplished the hybrid additive-subtractive laser powder bed fusion (h-LPBF) of a passive radio frequency (RF) component called a quarter wave cavity resonator (QWR). These QWR devices are high-value components with intricate features that find applications in strategic areas ranging from satellite communications to high energy physics. Given their complex internal geometry, QWRs are currently assembled from multiple components. While conventional LPBF has the ability to create these complex components as a monolithic part, poor frequency control and high RF losses due to geometric and finish issues prevent greater adoption. We show that h-LPBF overcomes the poor surface finish and geometric integrity of LPBF-processed QWR devices, thereby significantly improving their RF performance.

Specific conclusions are as follows:

- 1. Six QWR devices (material AlSi10Mg) were manufactured simultaneously on a Matsuura Lumex Avance 25 h-LPBF system. Three of these QWR devices were manufactured with conventional LPBF (no in-process machining), while three devices received subtractive machining on certain features critical to their function RF performance. The importance of these features was verified using theoretical RF simulations (COMSOL).
- 2. We demonstrate that the h-LPBF process improved the surface finish of these critical QWR features by a factor of 4 (Ra \sim 2 μ m to 3 μ m), compared to conventional LPBF (Ra \sim 6 μ m to 25 μ m), without loss of geometric integrity. As a consequence of these metrological improvements, the Q-factor of as-printed QWR devices made using h-LPBF is nearly double that of conventional LPBF devices; Q = 970 units vs. Q = 484 units, respectively.
- 3. The six QWR devices were post-processed to ameliorate their RF performance. Post-processing included stress relief followed by chemical etching. The electrical properties were re-measured after stress relief, and subsequent to chemical etching. Despite post-processing, the functional performance (Q-factor) of h-LPBF processed QWR resonators was nearly 1.5 to 2 times superior to the conventional LPBF counterparts. In other words, the functional improvement accrued by h-LPBF over conventional LPBF is maintained on post-process through stress relief and chemical etching.

In our future work, we will endeavor to scale the h-LPBF process to produce larger and more complex RF devices and waveguides and explore materials such as niobium and copper which can further enhance electrical properties. We also aim to conduct thorough analysis of the microstructure evolved, as an avenue towards understanding the effect of h-LPBF on material properties.

Statements and Declarations

a. Funding

The authors would like to thank Alexander Smirnov for assistance with the RF measurements as well as Pedro Frigola for overseeing the overall project scope. This work was supported by the U.S. Department of Energy, Office of High Energy Physics, under SBIR grant DE-SC0019973

Prahalada Rao thanks the National Science Foundation (NSF) and Department of Energy (DoE) for funding his work under awards OIA-1929172, CMMI-1920245, CMMI-1739696, ECCS-2020246, PFI-TT 2044710, CMMI-1752069, CMMI-1719388, and DE-SC0021136. Using the hybrid-LPBF process as a means to improve part quality was the major aspect of CMMI-1752069 (Program Officer: Kevin Chou). Supplemental funding for CMMI-1752069 was obtained through the NSF INTERN program (Program Officer: Prakash Balan) and CMMI Data Science Activities (Program Officer: Martha Dodson) is greatly appreciated. The latter supplement funded Ziyad Smoqi's research. The X-ray CT analysis was conducted on the instrument partially funded through the Major Research Instrumentation grant (CMMI-1920245, program officer: Wendy C. Crone). Alex Riensche's work was funded partially through the DoE Grant DE-SC0021136 and OIA-1929172.

b. Conflicts of interest/Competing interests

The authors have no relevant financial or non-financial interests to disclose.

c. Availability of data and material (data transparency)

Not Applicable.

d. Code availability (software application or custom code)

Note Applicable.

e. Ethics approval (include appropriate approvals or waivers)

Not Applicable.

f. Consent to participate (include appropriate statements)

Not Applicable.

g. Consent for publication (include appropriate statements)

Not Applicable

h. Author Contributions

All authors contributed to the study conception and design. Material preparation, data collection and analysis were performed by Alex Riensche, Paul Carriere and Prahalada Rao. Manufacturing of the part was carried out by Alex Riensche and Andrew Menendez. Measurements were carried out by Alex Riensche, Paul Carriere and Nanda Gopal Matavalam. Analysis and characterization was carried out by Aurora Araujo. Supervision was provided by Pedro Frigola and Sergey Kutsaev. The first draft of the manuscript was written by Alex Riensche and all authors commented on previous versions of the manuscript. All authors read and approved the final manuscript.

References

- [1] W.J. Sames, F.A. List, S. Pannala, R.R. Dehoff, S.S. Babu, The metallurgy and processing science of metal additive manufacturing, International Materials Reviews. 61 (2016) 315–360. https://doi.org/10.1080/09506608.2015.1116649.
- [2] D.R. Clymer, J. Cagan, J. Beuth, Power–Velocity Process Design Charts for Powder Bed Additive Manufacturing, Journal of Mechanical Design. 139 (2017). https://doi.org/10.1115/1.4037302.
- [3] J.C. Snyder, K.A. Thole, Understanding Laser Powder Bed Fusion Surface Roughness, Journal of Manufacturing Science and Engineering. 142 (2020). https://doi.org/10.1115/1.4046504.
- [4] T. DebRoy, H.L. Wei, J.S. Zuback, T. Mukherjee, J.W. Elmer, J.O. Milewski, A.M. Beese, A. Wilson-Heid, A. De, W. Zhang, Additive manufacturing of metallic components Process, structure and properties, Progress in Materials Science. 92 (2018) 112–224. https://doi.org/10.1016/J.PMATSCI.2017.10.001.
- P.R. Gradl, D.C. Tinker, J. Ivester, S.W. Skinner, T. Teasley, J.L. Bili, Geometric feature reproducibility for laser powder bed fusion (L-PBF) additive manufacturing with Inconel 718, Additive Manufacturing. 47 (2021) 102305. https://doi.org/10.1016/j.addma.2021.102305.
- [6] N.N. Kumbhar, A. V Mulay, Post Processing Methods used to Improve Surface Finish of Products which are Manufactured by Additive Manufacturing Technologies: A Review, Journal of The Institution of Engineers (India): Series C. 99 (2018) 481–487. https://doi.org/10.1007/s40032-016-0340-z.
- [7] X. Peng, L. Kong, J.Y.H. Fuh, H. Wang, A Review of Post-Processing Technologies in Additive Manufacturing, Journal of Manufacturing and Materials Processing. 5 (2021). https://doi.org/10.3390/jmmp5020038.

- [8] G.F. Benedict, Nontraditional Manufacturing Processes, CRC Press, 1987. https://doi.org/https://doi.org/10.1201/9780203745410.
- [9] V.K. Jain, Advanced (Non-traditional) Machining Processes Machining: Fundamentals and Recent Advances, in: J.P. Davim (Ed.), Springer London, London, 2008: pp. 299–327. https://doi.org/10.1007/978-1-84800-213-5_11.
- [10] M.P. Sealy, G. Madireddy, R.E. Williams, P. Rao, M. Toursangsaraki, Hybrid Processes in Additive Manufacturing, Journal of Manufacturing Science and Engineering. 140 (2018). https://doi.org/10.1115/1.4038644.
- [11] E.M. Sefene, Y.M. Hailu, A.A. Tsegaw, Metal hybrid additive manufacturing: state-of-the-art, Progress in Additive Manufacturing. (2022). https://doi.org/10.1007/s40964-022-00262-1.
- [12] D. Eisenbarth, M. Breuch, F. Soffel, K. Wegener, Challenges of combining direct metal deposition with milling for the fabrication of a rocket nozzle, in: Proceedings of the Special Interest Group Meeting on Advancing Precision in Additive Manufacturing, 2019: pp. 83–86.
- [13] W. Du, Q. Bai, B. Zhang, Machining characteristics of 18Ni-300 steel in additive/subtractive hybrid manufacturing, The International Journal of Advanced Manufacturing Technology. 95 (2018) 2509–2519. https://doi.org/10.1007/s00170-017-1364-0.
- [14] P. Wüst, A. Edelmann, R. Hellmann, Areal Surface Roughness Optimization of Maraging Steel Parts Produced by Hybrid Additive Manufacturing, Materials. 13 (2020). https://doi.org/10.3390/ma13020418.
- [15] S. Sarafan, P. Wanjara, J. Gholipour, F. Bernier, M. Osman, F. Sikan, M. Molavi-Zarandi, J. Soost, M. Brochu, Evaluation of Maraging Steel Produced Using Hybrid Additive/Subtractive Manufacturing, Journal of Manufacturing and Materials Processing. 5 (2021). https://doi.org/10.3390/jmmp5040107.
- [16] T. Torims, G. Pikurs, S. Gruber, M. Vretenar, A. Ratkus, M. Vedani, E. López, F. Brückner, First Proof-of-Concept Prototype of an Additive Manufactured Radio Frequency Quadrupole, Instruments. 5 (2021). https://doi.org/10.3390/instruments5040035.
- [17] H. Hähnel, U. Ratzinger, First 3D Printed IH-Type Linac Structure—Proof-of-Concept for Additive Manufacturing of Linac RF Cavities, Instruments. 6 (2022). https://doi.org/10.3390/instruments6010009.
- [18] P. Carriere, S. Kutsaev, A. Ronald, C.A. N, F. Pedro, T. Horn, M. Kelly, A. Smirnov, Fabrication Approaches to 3d Superconducting Qubit Resonators with a High Q-Factor, in: Bulletin of the American Physical Society, 2021: p. 66. https://ui.adsabs.harvard.edu/abs/2021APS..MARY30012C.
- [19] L. Ives, T. Bui, D. Marsden, G. Collins, T. Horn, C. Ledford, J. Neilson, Additive Manufacture of RF Loads for ITER, 2020. https://doi.org/10.1109/IVEC45766.2020.9520466.
- [20] A.H. Seltzman, S.J. Wukitch, Surface roughness and finishing techniques in selective laser

- melted GRCop-84 copper for an additive manufactured lower hybrid current drive launcher, Fusion Engineering and Design. 160 (2020) 111801. https://doi.org/10.1016/j.fusengdes.2020.111801.
- [21] S. Sirci, E. Menargues, M. Billod, Space-qualified Additive Manufacturing and its Application to Active Antenna Harmonic Filters, in: 2021 IEEE MTT-S International Microwave Filter Workshop (IMFW), 2021: pp. 239–242. https://doi.org/10.1109/IMFW49589.2021.9642306.
- [22] S.S. Gill, H. Arora, Jidesh, V. Sheth, On the development of Antenna feed array for space applications by additive manufacturing technique, Additive Manufacturing. 17 (2017) 39–46. https://doi.org/doi.org/10.1016/j.addma.2017.06.010.
- [23] R.R. Mansour, High-Q tunable dielectric resonator filters, IEEE Microwave Magazine. 10 (2009) 84–98. https://doi.org/10.1109/MMM.2009.933591.
- [24] J.C. Fox, S.P. Moylan, B.M. Lane, Effect of Process Parameters on the Surface Roughness of Overhanging Structures in Laser Powder Bed Fusion Additive Manufacturing, Procedia CIRP. 45 (2016) 131–134. https://doi.org/10.1016/j.procir.2016.02.347.
- [25] S. V Kutsaev, K. Taletski, R. Agustsson, P. Carriere, A.N. Cleland, Z.A. Conway, É. Dumur, A. Moro, A.Y. Smirnov, Niobium quarter-wave resonator with the optimized shape for quantum information systems, EPJ Quantum Technology. 7 (2020) 7. https://doi.org/10.1140/epjqt/s40507-020-00082-8.
- [26] N.T. Aboulkhair, M. Simonelli, L. Parry, I. Ashcroft, C. Tuck, R. Hague, 3D printing of Aluminium alloys: Additive Manufacturing of Aluminium alloys using selective laser melting, Progress in Materials Science. 106 (2019) 100578. https://doi.org/10.1016/j.pmatsci.2019.100578.
- [27] M. Tang, Inclusions, Porosity, and Fatigue of AlSi10Mg Parts Produced by Selective Laser Melting, Ph.D presentation, Carnegie Mellon University, 2017.
- [28] N. Clark, S. Hefford, A. Porch, Effect of build orientation and surface finish on surface resistance in microwave components produced by Selective Laser Melting, in: 2017 47th European Microwave Conference (EuMC), 2017: pp. 508–511. https://doi.org/10.23919/EuMC.2017.8230901.
- [29] R. Gumbleton, K. Nai, S. Hefford, A. Porch, Effects of Post-Processing Treatments on the Microwave Performance of Additively Manufactured Samples, in: 2019 13th European Conference on Antennas and Propagation (EuCAP), 2019: pp. 1–4.
- [30] B. Curran, I. Ndip, S. Guttowski, H. Reichl, On the quantification and improvement of the models for surface roughness, in: 2009 IEEE Workshop on Signal Propagation on Interconnects, 2009: pp. 1–4. https://doi.org/10.1109/SPI.2009.5089851.
- [31] E. Hammerstad, O. Jensen, Accurate Models for Microstrip Computer-Aided Design, in: 1980 IEEE MTT-S International Microwave Symposium Digest, 1980: pp. 407–409. https://doi.org/10.1109/MWSYM.1980.1124303.
- [32] A. Townsend, N. Senin, L. Blunt, R.K. Leach, J.S. Taylor, Surface texture metrology for metal additive manufacturing: a review, Precision Engineering. 46 (2016) 34–47.

- https://doi.org/10.1016/J.PRECISIONENG.2016.06.001.
- [33] S. Ramo, J.R. Whinnery, T. Van Duzer, Fields And Waves In Communication Electronics, 3rd ed., John Wiley & Sons, Inc., 1994.
- [34] Lumex Avance Hybrid Metal 3D Printer, (n.d.). https://www.lumex-matsuura.com/english/(accessed February 2, 2022).
- [35] C. Silbernagel, I. Ashcroft, P. Dickens, M. Galea, Electrical resistivity of additively manufactured AlSi10Mg for use in electric motors, Additive Manufacturing. 21 (2018) 395–403. https://doi.org/https://doi.org/10.1016/j.addma.2018.03.027.
- [36] Z. Smoqi, A. Gaikwad, B. Bevans, M.H. Kobir, J. Craig, A. Abul-Haj, A. Peralta, P. Rao, Monitoring and prediction of porosity in laser powder bed fusion using physics-informed meltpool signatures and machine learning, Journal of Materials Processing Technology. 304 (2022) 117550. https://doi.org/https://doi.org/10.1016/j.jmatprotec.2022.117550.
- [37] D. Kajfez, Linear fractional curve fitting for measurement of high Q factors, IEEE Transactions on Microwave Theory and Techniques. 42 (1994) 1149–1153. https://doi.org/10.1109/22.299749.
- [38] R. Subramanian, D. Rule, O. Nazik, Dependence of LPBF Surface Roughness on Laser Incidence Angle and Component Build Orientation, (2021). https://doi.org/10.1115/GT2021-59755.